Revisiting Compositional Accuracy of Carbides Using a Decreased Detector Efficiency in a LEAP 6000 XR Atom Probe Instrument

Microscopy and Microanalysis, 2024, **00**, 1–9
https://doi.org/10.1093/mam/ozae069

Original Article

Microscopy AND Microanalysis

Revisiting Compositional Accuracy of Carbides Using a Decreased Detector Efficiency in a LEAP 6000 XR Atom Probe Instrument

Severin Jakob*, and Mattias Thuvander*

Department of Physics, Chalmers University of Technology, SE-412 96 Göteborg, Sweden

***Corresponding authors:** Severin Jakob, E-mail: severin.jakob@chalmers.se; Mattias Thuvander, E-mail: mattias.thuvander@chalmers.se

Abstract

The accuracy of carbon composition measurement of carbide precipitates in steel or other alloys is limited by the evaporation characteristics of carbon and the performance of current detector systems. Carbon evaporates in a higher fraction as clustered ions leading to detector pile-up during so-called multiple hits. To achieve higher accuracy, a grid was positioned behind the local electrode, reducing the detection efficiency from 52 to 7% and thereby reducing the fraction of multi-hit events. This work confirms the preferential loss of carbon due to detector pile-up. Furthermore, we demonstrate that the newer generation of commercial atom probe instruments displays somewhat higher discrepancy of carbon composition than previous generations. The reason for this might be different laser–matter interaction leading to less metal ions in multi-hit events.

Key words: atom probe tomography, carbides, detection efficiency, detector pile-up

Graphical Abstract

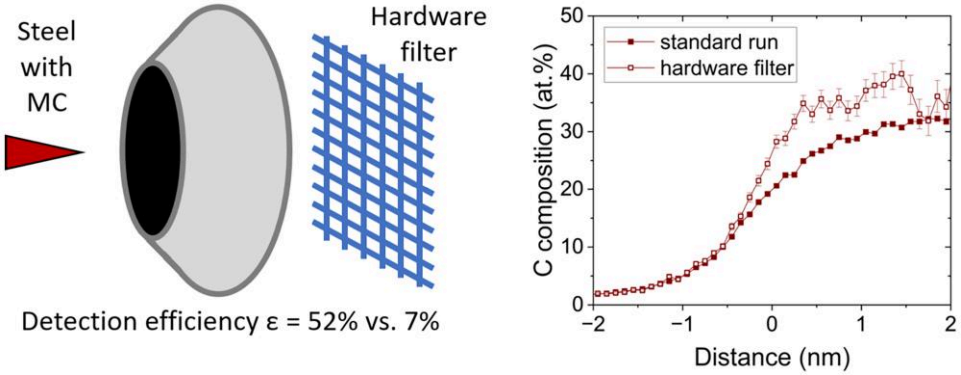

Introduction

Atom probe tomography (APT) is a powerful tool for the investigation of local chemistry of materials at the nanoscale (Larson et al., 2013; Miller & Forbes, 2014). The technique has almost atomic resolution and high sensitivity for all elements. The specimen, which is a needle-shaped tip, is held at a high DC voltage. Ions are field evaporated by an additional voltage- or laser-pulse and identified by time-of-flight mass spectroscopy. The ions are accelerated by the high voltage and fly toward a position-sensitive detector. A reconstruction algorithm works out the x and y coordinates of the atoms from the impact position on the detector. The z coordinate is calculated from the ion sequence resulting in a reconstructed volume of the material, with position and identity of the detected atoms/ions.

A high detection efficiency is desired to represent the material in the most realistic way; in this way, minimizing the error bars of feature compositions as well as enabling more accurate cluster finding and chemistry (Stephenson et al., 2011). The detector efficiency, however, is limited mostly by the open area of the instrumentation in the ions' flight path. The detectors of recent generations of commercial local electrode atom probes (LEAP® 5000 and 6000) have a multichannel plate that has an open area of 80%. The microchannel plate turns the impact of ions into electron cascades. The electrons are collected by three delay lines that are rotated relative to each other. A timed readout of the delay line signals yields the position of ion impact. Often the atom probe instrument is equipped with a reflectron for higher mass resolution. The reflectron consists of a wire mesh held at a positive voltage that bends the trajectory of the

Received: March 11, 2024. **Revised:** May 31, 2024. **Accepted:** July 4, 2024

ions toward the detector, while compensating energy deficits or excesses. The transmission is reduced again leading to a detection efficiency of 52% for modern LEAP instruments.

If more than one hit occurs in close proximity in time and space, the detector system is not able to distinguish between hits (Rolander & Andrén, 1989; Da Costa et al., 2005; Prosa & Oltman, 2022). This is referred to as the dead-time of the detector or a detector pile-up (Ismail et al., 2005; Stephan et al., 2015). In the case of multiple ions hitting the detector from the same pulse, only the impacts, which can be attributed to a certain position and time of flight, are registered. These are called multiple hits. The number of ions hitting within the limits of dead-time and -distance of the detector is not known and these ions are lost due to the detector pile-up. It is common practice to use low detection rates to avoid multiple-ion emission (Rolander & Andrén, 1994). However, certain elements as well as microstructural features are prone to correlated evaporation (De Geuser et al., 2007). Compositional accuracy is limited for certain elements or compounds. Carbon or carbides usually show a reduced composition (Yao et al., 2010; Thuvander et al., 2011; Lewis et al., 2015; Peng et al., 2018) with the exception of cementite, where too high C composition has been found (Takahashi et al., 2011). This is attributed to preferential Fe loss (Marceau et al., 2013; Kitaguchi et al., 2014). In some cases, an isotope with smaller natural abundance can be used to compensate the underestimation of the carbon composition, since the effect of dead-time is much stronger for large peaks (^{12}C) than for small peaks (^{13}C) (Thuvander et al., 2011). The electrostatic field, and hence the used laser pulse energy (LPE), has an influence on the apparent composition (Mancini et al., 2014; Peng et al., 2017; Baik et al., 2018). Composition measurements are similarly limited for boron (Da Costa et al., 2012; Meisenkothen et al., 2015), nitrides (Tang et al., 2010; Morris et al., 2022; Schiester et al., 2024) as well as other compounds (Müller et al., 2011; Kinno et al., 2012).

The reduction of detector efficiency has proven to decrease the fraction of multiple hits, therefore improving the accuracy of composition measurements of carbides (Thuvander et al., 2013, 2019) as well as nitrides (Schiester et al., 2024). In these works, the detector efficiency was reduced by a mesh in the ion flight path. This hardware filtering has a transmission of only 14% and hence the detection efficiency is decreased to $0.14 \times 52\% = 7\%$. The aim of this work is to quantify the effect of using the same hardware filtering as previously used on the newest generation of LEAP instrument. The investigation on the same steel as was used in Thuvander et al. (2019) allows for a direct comparison between a LEAP 3000X HR with 37% detector efficiency and a green laser wavelength (532 nm), and a LEAP 6000 XR with deep-UV laser light (258 nm) and a detection efficiency of 52%.

Materials and Methods

The investigated material is a precipitation hardened steel with composition of 0.3Si–2.6Cr–0.8Mn–2.2Mo–0.9V–0.4C (wt %). This is the same material as was used previously for quantifying C with reduced detection efficiency and was labeled Steel B in Thuvander et al. (2019). After austenitization, the steel was tempered two times for 2 h at 625°C to form secondary carbides. The carbides are of MC type with similar amounts of Mo and V, and some Cr. The expected stoichiometry is therefore 50 at% C. For carbides of type M_2C, the Mo/V ratio should be higher (Andersson, 2011).

Matchstick specimens with dimensions of $0.3 \times 0.3 \times 15$ mm^3 were fabricated by cutting and grinding. Then a two-step electro-polishing was performed in 10% perchloric acid and 2% perchloric acid to obtain sharp needlelike tips (Lefebvre-Ulrikson et al., 2016). APT measurements were done on a LEAP 6000 XR (CAMECA Inc., Madison, WI, USA) in laser-mode with 30 pJ LPE at 200 kHz pulse frequency and 50 K test temperature. On the one hand, experiments with a standard local electrode with 30 μm hole diameter were conducted. These experiments will be called normal local electrode (NLE) runs. The detection rate for the NLE runs was set to 0.5%. On the other hand, specimens of the same material were measured with reduced detection efficiency. This was achieved by placing a grid on the backside of a local electrode assembly and hence in the path of the accelerated ions. The grid has 14% open area where ions can pass to the detector. Combining this with 52% detection efficiency of the APT instrument results in an effective detection efficiency of 7%. This gridded local electrode (GLE) has a 40 μm diameter hole and is the same local electrode as in previous papers (Schiester et al., 2024; Thuvander et al., 2013, 2019). The different hole diameter is due to a change from 40 to 30 μm for the newer generation of LEAP instruments. To emulate a similar evaporation field for experiments at reduced detection efficiency, the detection rate was set to 0.07–0.1% for the GLE experiments. One experiment is extensively presented in the main article and additional specimens are depicted in the Supplementary Material. To investigate the electrostatic field during laser-assisted evaporation of this material and the influence of LPE, measurements of this steel were conducted with the NLE using LPEs of 15–60 pJ. Since the $^{56}Fe^{+}$ peak had limited counts in all experiments and an overlap with MoC^{++}, charge state ratios (CSRs) of the ^{98}Mo isotope in double- and triple-charged condition were recorded. An estimate of the electrostatic field was calculated according to the fitting parameters in Tegg et al. (2024), which are based on the well-known Kingham curves (Kingham, 1982).

Additionally, specimens made from hybrid steel (Ovako AB, Sweden), that were previously measured in voltage mode on the LEAP 3000X HR, were used for analysis of multiples and compared to voltage runs on the LEAP 6000 XR. This material precipitates intermetallic NiAl particles and Cr-rich carbides. Details about the material can be found in Jakob et al. (2024). The measurement parameters on the LEAP 3000X HR were 0.2% detection rate, 200 kHz pulse frequency, and 80 K test temperature. Experiments on the LEAP 6000 XR were conducted with a virtually same detection rate of $0.2\% \times 0.52\%/0.37\% = 0.28\%$ and 80 K test temperature at 200 kHz pulse frequency. Further measurements were performed with 0.5–1% detection rate and 70 K test temperature at 100–333 kHz pulse frequency. All voltage experiments were performed with 20% voltage pulse.

The analysis was done with the commercial software AP Suite 6.3 as well as custom scripts in MATLAB R2021b to extract the multiplicity from APT data. The APT software registers the first ion in a multi-hit event as the "multiple" and assigns a multiplicity $n > 1$ to the ion. The following *n-1* ions of the same pulse have multiplicity 0, but belong to the same multi-hit event. AP Suite designates ions with multiplicity 0 as "partials", however, these ions meet the criterion of at least five out of six delay line signals, making it possible to

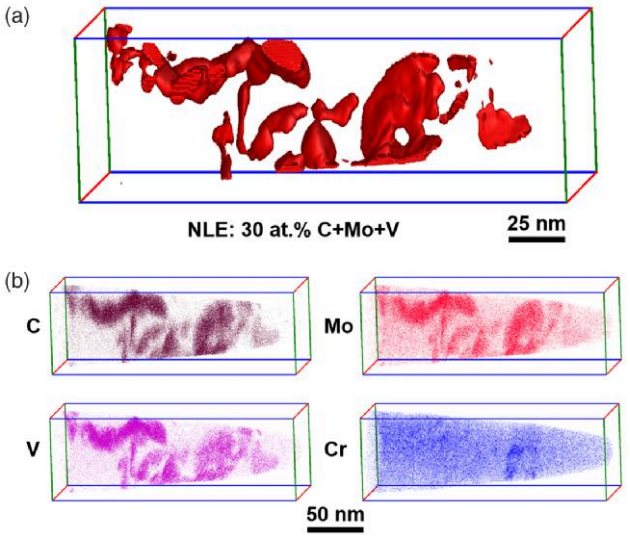

Fig. 1. Reconstruction of a specimen from the NLE reference measurement. (**a**) Iso-surfaces with a threshold value of 30 at% C + Mo + V and (**b**) the carbide-forming elements C, Mo, V, and Cr are shown.

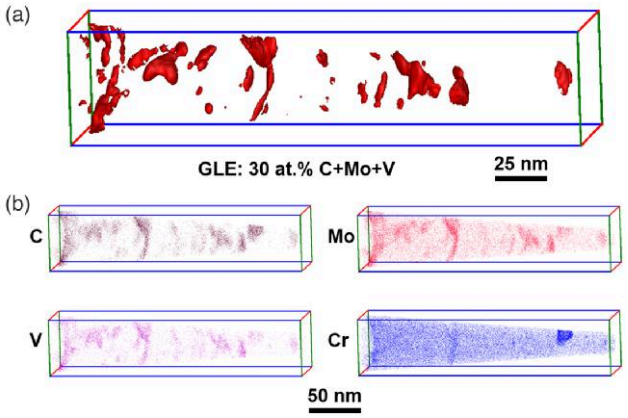

Fig. 2. Reconstruction of specimen 1 from the GLE measurements. (**a**) Iso-surfaces with a threshold value of 30 at% C + Mo + V and (**b**) the carbide-forming elements C, Mo, V, and Cr are shown. The Cr-rich carbide near the apex of the tip was excluded from the comparison between runs.

determine mass and position. This should not be confused with "unrecoverable partials", which are uncertain in time and space and therefore ignored (Larson et al., 2013). Throughout the manuscript, only the term "multiples" will be used and means ions which were successfully registered by the APT software during multi-hit events. For iso-concentration surfaces, the voxel size was 1.0 nm^3 and the de-localization was $3.0 \times 3.0 \times 1.5$ nm^3.

Results

Figure 1 shows the reconstruction of the NLE reference run. The carbides were separated from the rest of the measurement for further analysis by iso-concentration surfaces, also known as iso-surfaces, of 30 at% C + Mo + V (Fig. 1a), as was done in Thuvander et al. (2019). In this way, a direct comparison to the previously used LEAP 3000X HR instrument is possible. Figure 1b shows atom distributions of carbide-forming elements. Except for Cr, the elements are equally distributed to the carbides. The GLE run of specimen 1 is displayed in Figure 2. Further experiments are presented in the Supplementary Material. Iso-surfaces with the same threshold value are depicted in Figure 2a as well as the same carbide-forming elements in Figure 2b. Apart from the expected Mo and V-rich carbides, a Cr-rich region can be seen. The latter was most probably a cementite particle that gained a Cr-rich shell during the heat treatment. An iso-surface on the inner bound of the Cr shell was used to draw the proxigram in Figure 3. This carbide was excluded for the comparison of Mo/V-carbides between the NLE and the GLE experiments.

The mass spectra of both experiments do not show any difference in terms of ion species or relative amounts. Figure 4 shows the mass spectra for the carbide regions, isolated by the iso-surfaces. The ion count difference between the NLE run (Fig. 4a) and the GLE run (Fig. 4b) resulting from the reduced detection efficiency can be seen in the difference of one order of magnitude on the *y* axis. Ions from carbide-forming elements such as V, Mo, and C are obviously higher for the subset within the iso-surfaces than in the overall mass spectra (not shown here). Only slight differences in the metal contents are visible between the NLE and GLE runs. Figure 5 shows the mass spectra of ions from multi-hits within the carbide subsets. Note that in this case, the *y* axis is different by two orders of magnitude, meaning that a higher proportion of multiples was eliminated by the grid. The highest count of multiples comes from C^{++}, followed by C^{+}, then $(M = V \text{ or } Cr)^{++}$ and C_2^{+} in similar amounts, followed by Fe^{++}, C_3^{++}, Mo^{+++}/Mo^{++}, and C_3^{+}. Multiples of MoC^{++} were more prominent for the NLE run (Fig. 5a) than for the GLE run, where only a few such multiples were found (Fig. 5b).

Figure 6 shows the fraction of multi-hit events as a function of multiplicity for the experiments. The columns are divided into matrix ions and ions from the carbide subsets. The NLE run had 98.8% single and 1.2% multi-hit events in the matrix. However, the carbide subset consisted of 84.3% singles and 15.7% multi-hits. The GLE run had 99.6% single and 0.4% multi-hit events in the matrix. The carbide subset of the GLE run contained 95.0% singles and only 5.0% multi-hits. The same kind of experiment on the LEAP 3000X HR showed 20.5 and 2.6% multi-hits in the carbide subset during the NLE run and GLE run, respectively (Thuvander et al., 2019).

Table 1 shows the fraction of ions from multi-hit events within the carbide subsets for the carbide-forming elements. On the one hand, the NLE run records 76.5% of C and 50.2% of Mo in multiples. Cr and V have a multiples fraction of about 25 and 21%, Fe has 13.5%. On the other hand, C multiples have a fraction of about 17.7% in the GLE run. Furthermore, the relative amount of multiples from the metals is significantly reduced and even as low as 3.2% for Fe. The comparison to literature shows similar fractions of multiples for C between NLE runs. However, the fractions of metal ions coming in multi-hit events are lower for LEAP 6000 XR as compared to LEAP 3000X HR in NLE and GLE runs. Note that the number of lost ions is not proportional to the recorded fractions, since more than one extra ion could be lost in the detector pile-up.

Figure 7a shows the proxigram of 30 at% (C + Mo + V) iso-surfaces in the NLE run. The C composition is approaching a value of about 32 at% with about 30 at% Mo and 15 at% Cr and V each. Figure 7b displays the proxigram of the corresponding iso-surfaces in the GLE run. In this case, the C

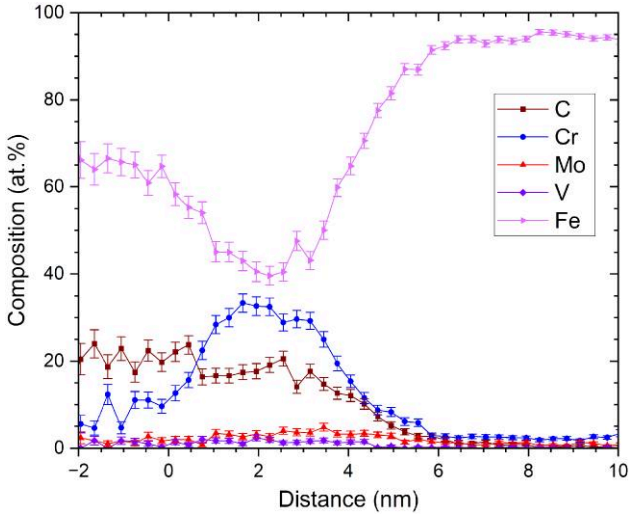

Fig. 3. Proxigram of the Cr-rich carbide near the apex of the tip of the GLE run shown in Figure 2. The core region is to the left in the diagram.

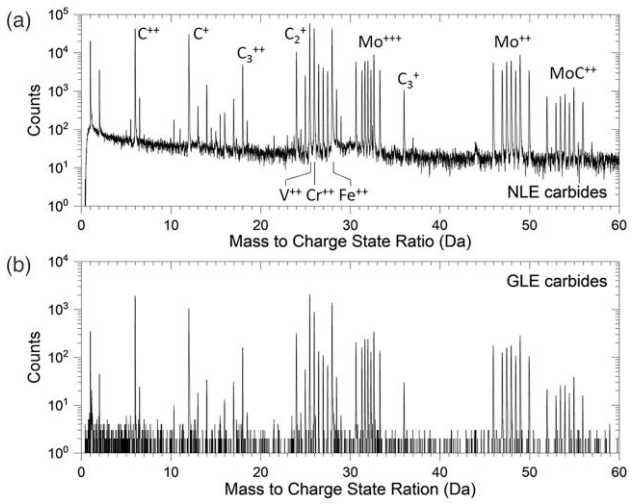

Fig. 4. Mass spectra of the carbide regions of (**a**) NLE and (**b**) GLE runs.

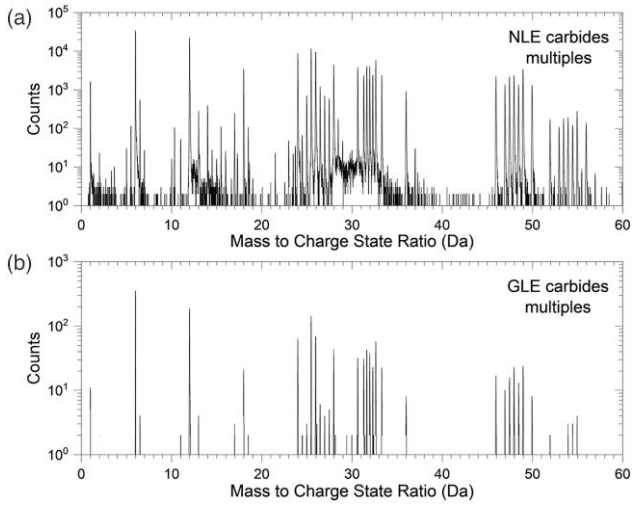

Fig. 5. Mass spectra of ions recorded in multi-hit events in the carbide regions of (**a**) NLE and (**b**) GLE runs.

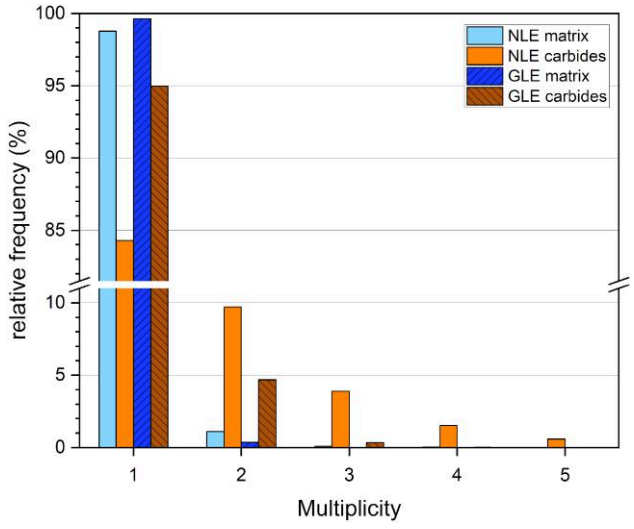

Fig. 6. Frequency histogram of single and multi-hit events for NLE and GLE runs, matrix, and carbide regions, respectively.

composition approaches 40 at%. Note the larger error bars due to the limited number of sampled ions. Mo and V display similar values as the NLE run, whereas Cr has lower composition in the GLE run. The lower amount of Cr might be explained by the Cr-rich carbide being in close proximity to the other carbides. The composition within the iso-surface was calculated using the peak decomposition tool in AP Suite. The algorithm calculates the contributions to a peak in the mass spectrum where different elements pose an overlap based on the natural abundance of the other isotopes of the involved elements. The occurring peak overlaps are explained in the Discussion. The compositions are displayed with and without contribution of Fe in Table 2 to show the contribution of Fe due to the local magnification effect (Miller & Hetherington, 1991; Vurpillot et al., 2000).

Figure 8 shows a comparison of the C composition between NLE and GLE runs (proxigrams). The data from Thuvander et al. (2019) is included as well. The direct comparison of GLE and NLE runs shows the significant effect that the reduction in multiples has on the measured composition. In the NLE run, C reaches a plateau value of about 32 at%, whereas with the hardware filter, the plateau is located at about 40 at %. The plateau value of C composition even approaches the stoichiometric value of 50 at% in a large carbide during the GLE run of specimen 2 (see Supplementary Figs. S1, S2). The comparison between different LEAP generations shows, on the one hand, that the NLE run from the LEAP 3000X HR has higher C composition than the run from the LEAP 6000 XR. On the other hand, the GLE runs depict similar C composition within the carbides.

The carbides in this material have a higher evaporation field than the matrix (Leitner et al., 2004; Thuvander et al., 2011). Therefore, the carbides appear bigger than they actually are due to the local magnification effect (Miller & Hetherington, 1991; Vurpillot et al., 2000). Moreover, the carbides appear to have less atomic density than the matrix as can be seen in Figure 9, which is consistent with the effect of local

Table 1. Fraction of Ions Recorded in Multiple Events in the Carbide Regions and Comparison to Literature.

	C	V	Cr	Fe	Mo
NLE, LEAP 6000 XR this work	76.5	21.4	25.2	13.5	50.2
GLE, LEAP 6000 XR this work	17.7	6.7	7.5	3.2	11.6
NLE, LEAP 3000X HR (Thuvander et al., 2019)	66–82	41			57
GLE, LEAP 3000X HR (Thuvander et al., 2019)	27–34	28			30
NLE, LEAP 3000X HR (Martin et al., 2017)	74.3				
NLE, LEAP 5000 XR (Martin et al., 2017)	85.9				

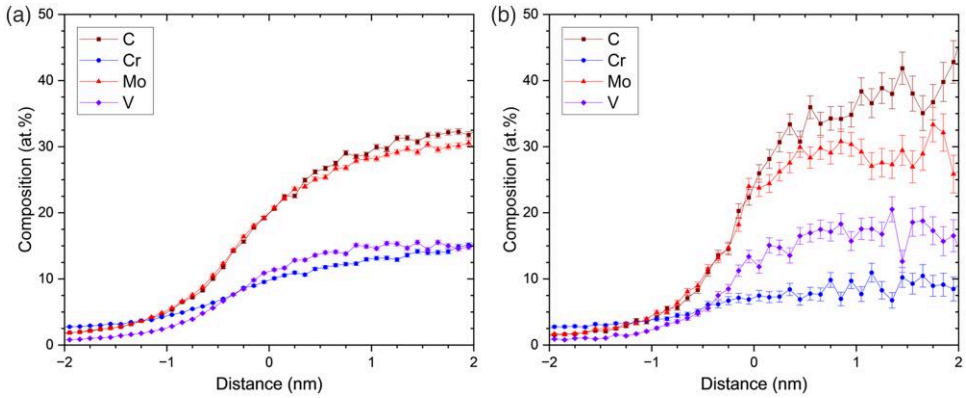

Fig. 7. Proxigrams of the 30 at% C + Mo + V iso-surfaces for the (**a**) NLE and (**b**) GLE runs.

Table 2. Composition Within the Carbide Regions.

		C	V	Cr	Fe	Mo
LEAP 6000 XR	NLE	31.1 ± 0.1	14.5 ± 0.1	13.6 ± 0.1	12.5 ± 0.1	28.4 ± 0.1
	NLE w/o Fe	35.2 ± 0.1	16.4 ± 0.1	16.2 ± 0.1	-	32.1 ± 0.1
	GLE	38.6 ± 1.4	14.6 ± 0.3	7.8 ± 0.2	12.0 ± 0.3	26.6 ± 0.4
	GLE w/o Fe	43.6 ± 1.6	16.8 ± 0.4	9.6 ± 0.3	-	29.9 ± 0.5
LEAP 3000X HR (Thuvander et al., 2019)	NLE	31.4 ± 0.8	18.8 ± 1.0	10.9 ± 1.4	13.4 ± 1.2	22.7 ± 0.9
	NLE w/o Fe	37.5 ± 1.0	22.4 ± 1.2	13.0 ± 1.7	-	27.1 ± 1.1
	GLE	33.0 ± 1.4	17.0 ± 1.9	8.6 ± 2.7	17.8 ± 1.9	16.6 ± 2.0
	GLE w/o Fe	43.8 ± 1.8	22.6 ± 2.5	11.4 ± 3.6	-	22.1 ± 2.7

magnification (Leitner et al., 2004). The arrow in Figure 9 points at the location of the Cr-rich carbide. The similar density inside the carbide as in the matrix further indicates that it is a primary cementite particle. Note that the difference between the density values for the GLE and NLE runs corresponds to the fraction of open area of the hardware filter.

The influence of LPE was investigated in NLE experiments using the LEAP 6000 XR instrument. Figure 10a shows reconstructions of about 4–5 million ions each for LPEs between 15 and 60 pJ. A total of 30 at% (C + Mo + V) iso-surfaces are depicted as well as a portion of Mo atoms for illustration. Figure 10b depicts the proxigrams of the iso-surfaces and includes the NLE reference run as well. The evaporated volumes during 15 and 30 pJ contained only smaller carbides and hence limited data in the proxigrams. Figure 10c shows the C composition as the average between 0.9 and 1.3 nm of the proxigrams shown in Figure 10b. The C composition displays a general trend to higher values with higher LPE. Figure 10c shows the fraction of pulses with a multi-hit event during evaporation for the overall measurements as well as within the carbide regions. The multi-hit fraction is generally decreasing with higher LPE, except for 60 pJ.

To gain insight into the actual electrostatic field during evaporation, the CSRs of the ^{98}Mo isotope were recorded. Figure 11 shows the CSRs for the LPE variation of the NLE experiments, the measurements from Thuvander et al. (2019), the NLE and GLE runs as well as voltage NLE runs. The field estimate was calculated with the parameters presented in Tegg et al. (2024) and lies between 35.6 and 37.0 V/nm for the laser measurements. The local electrostatic field within the carbides is depicted with star-shaped symbols and consistently higher than the overall field as is expected for these MC-type carbides. The field varies within 1 V/nm for the carbide regions during all laser experiments. The experiments on the LEAP 3000X HR depict slightly lower CSRs than the experiments on the newer instrument. During NLE voltage runs the overall CSR was higher than for the LEAP 3000X HR run. The estimated field within the carbide regions is higher than during laser runs and rather similar between the instruments and measurement parameters.

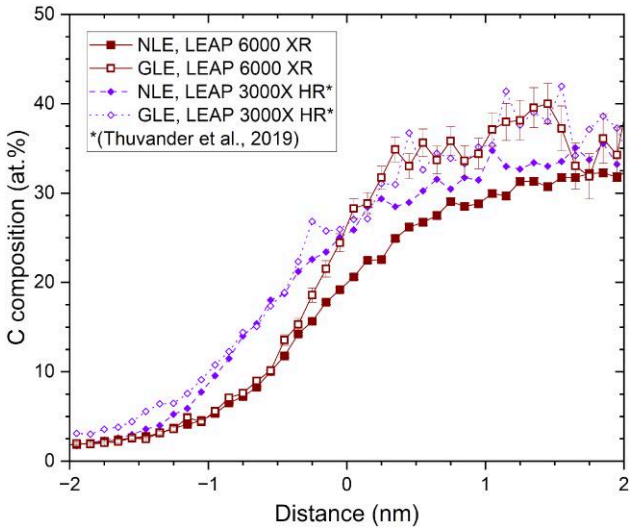

Fig. 8. Proxigrams showing the comparison of C composition between NLE and GLE measurements as well as previous measurements on a LEAP 3000X HR.

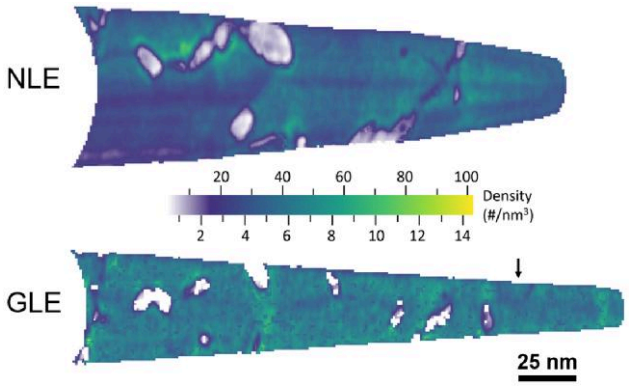

Fig. 9. Density maps of 5 nm thick slices of the reconstructions of the NLE and GLE experiments. Note the different color code values for NLE and GLE experiments. The arrow points at the position of the Cr-rich carbide showing similar density as the matrix.

Discussion

The LEAP 6000 XR has been used to measure the C composition with and without a hardware filter, specifically a grid placed behind a local electrode (GLE runs), to reduce the detection efficiency and, hence, the fraction of multi-hit events at the detector. This instrument uses the same detector system as the LEAP 5000 series but has a deep-UV laser. The detector efficiency is 52% for the reflectron-equipped instrument used here. In comparison to the LEAP 3000X HR, which has 37% detection efficiency, the detection algorithm has been updated, according to the instrument supplier. For details regarding the performance of the detector system, see Prosa & Oltman (2022).

The reconstruction of the NLE reference run has 25.4 million recorded ions. The GLE run of specimen 1, presented extensively here, contains 1.8 million, which corresponds to virtually 12.7 million ions without the grid. Further GLE experiments are shown in the Supplementary Material. Several carbides were present in each of the measured volumes for both NLE and GLE runs, hence a valid comparison is possible. The 24 Da peak was assigned as C_2^+, however, there is certainly a fraction of C_4^{++} present since a small peak at 24.5 Da is visible. The peak at 27 Da stems from $^{54}Cr^{++}$ and $^{54}Fe^{++}$. Considering the natural abundances, this peak was ranged as Fe, however, within the carbide subset a significant fraction of this peak corresponds to Cr. Another overlap might be between $^{96}Mo^{++}$ and C_4^+. The peak-shape as well as the natural abundance of Mo isotopes indicates that there was no significant contribution of C_4^+, and the peak was therefore ranged as Mo. The compositions in Table 2 were calculated with the peak decomposition tool in AP Suite, where the contribution of different elements to a peak overlap is calculated based on the natural abundance of the other isotopes. The C composition is in between values with the 24 Da peak ranged as C_2^+ or C_4^{++}.

The mass spectra of NLE and GLE runs show no significant differences. This indicates that the electrostatic field strengths during experiments were similar between the runs, as was confirmed by the CSRs. The detection rates for the GLE experiments were specifically reduced to imitate a similar electrostatic field to the NLE runs during evaporation. Furthermore, both the NLE run as well as the GLE experiments display reduced ion density within the carbides as expected for high-field phases. The field estimate of the carbide regions during LPE variation correlates well with the fraction of multi-ion evaporation events shown in Figure 10c. A general trend of improved C composition at higher LPE is observed. The same phenomenon was shown for tungsten carbide where a reduced fraction of multiples and slightly improved composition was achieved at higher LPEs (Peng et al., 2017). This is in contrast to the observation of Baik et al. (2018) on Cr carbides, where higher LPE led to lower C composition. They discuss that molecular ions and shifting peak overlaps might be the reason for the change in C composition. LPEs of 45 and 60 pJ within this work led to surface segregation of Si toward crystallographic poles. This is known as directional walk and indicates too high thermal pulsing of the specimens (Gault et al., 2010, 2012; Hyde et al., 2011).

The measurement of the same steel sample material as in an earlier study on the LEAP 3000X HR makes a direct comparison between the measurements of carbides in the different instruments, as well as with reduced detection efficiency, possible (Thuvander et al., 2019). The fraction of multi-hits in the carbide subsets is reduced from 20.5 to 15.7%, for LEAP 3000X HR and LEAP 6000 XR, respectively. Reducing the detection efficiency by a hardware filter, as was done with the GLE, showed a strong reduction of multi-hit events. The carbide subset contained 5.0% multi-hits for the GLE run in this paper, compared to 2.6% on the LEAP 3000X HR. The majority of multiples are C ions and compounds as can be seen in the mass spectra in Figure 5. The comparison to previous measurements of multiples, as depicted in Table 1, shows similar multiple fractions for C between different LEAP instruments (NLE runs). The multiple fraction of C of 76.5% for the NLE run does not constitute a significant increase between LEAP generations as was observed by Martin et al. (2017) for a LEAP 5000 XR instrument. A different steel was investigated in their work and therefore a direct comparison might not be accurate. From the comparison between the same steel in Table 1, it is, however, evident that a lot fewer metal ions are recorded as multiples than previously. The fraction of Mo ions in multiple events is slightly reduced from 57 to 50%, however, only 21.4% of the V ions were recorded in multiple events as opposed to 41% in the LEAP 3000X HR.

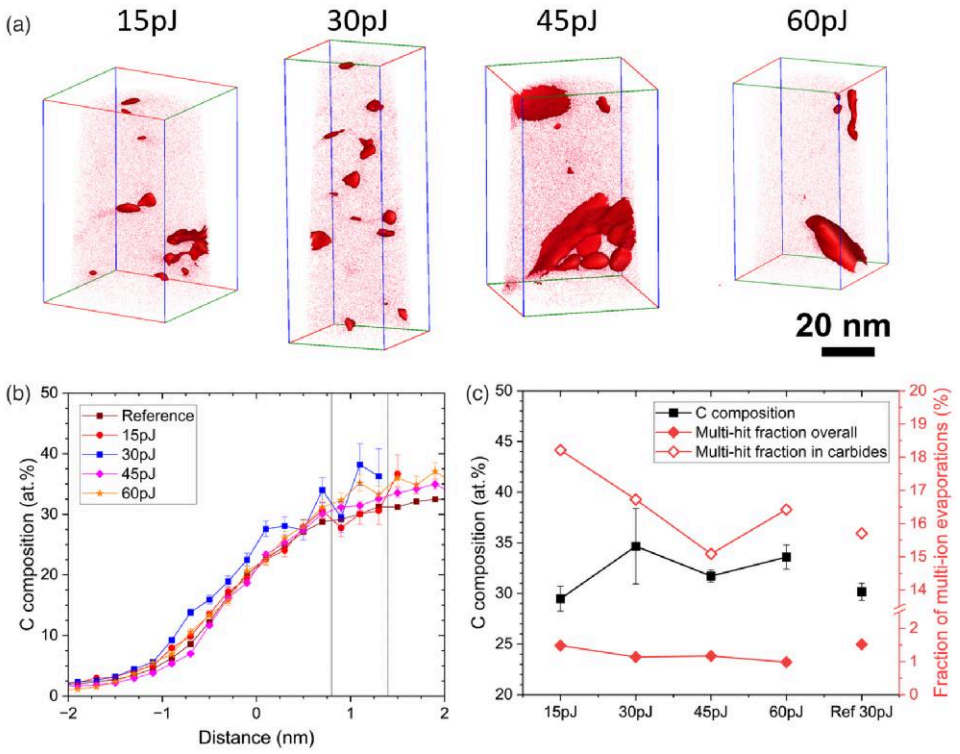

Fig. 10. (**a**) Reconstructions of NLE measurements with different LPE; Mo atoms as well as 30 at% (C + Mo + V) iso-surfaces are shown; (**b**) proxigrams of the iso-surfaces shown in (**a**); the C composition of the NLE reference run is included as well; (**c**) shows the average C composition at a distance between 0.9 and 1.3 nm of the iso-surfaces as well as fractions of multi-hit evaporation events in the overall reconstruction and the carbide regions.

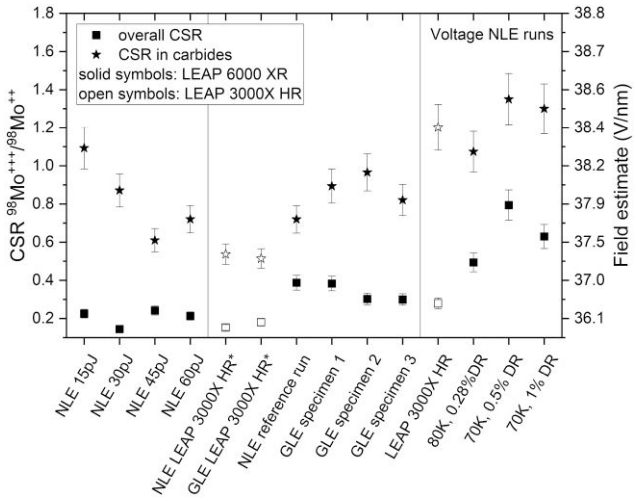

Fig. 11. $^{98}Mo^{+++}/^{98}Mo^{++}$ CSRs and electrostatic field estimates according to Tegg et al. (2024) of experiments within this study and Thuvander et al. (2019)—indicated by asterisks; note that the scale on the secondary *y* axis is nonlinear. For further information, see the text.

The use of a hardware filter in the LEAP 3000X HR reduced the fraction of multiples to similar amounts of 27–34% for C and metals alike. This study shows that the fraction of multiples in the LEAP 6000 XR is significantly lower, especially for metal ions. The use of a GLE reduces the fraction of multiples to 17.7% for C, 11.6% for Mo, about 7% for V and Cr, and 3.2% for Fe.

The accuracy of the C compositions between NLE and GLE as well as measurements on the LEAP 6000 XR compared to a LEAP 3000X HR is displayed in Figure 8. It is evident that the measurement with an NLE results in an increased preferential loss of C for the new instrument. The compositions of carbides contain about 35 at% of C for the LEAP 3000X HR whereas only about 32 at% C in the new instrument for the NLE runs. This was also observed for the LEAP 5000 XR (Martin et al., 2017). They speculated that the improved algorithm of the detector system for the LEAP 5000 (and LEAP 6000) favors Fe detection. Cuduvally et al. (2023) similarly report lower C fraction in a stochiometric SiC semiconductor device for a LEAP 5000 XS compared to a LEAP 4000X HR instrument. They found a high propensity of C in multiple events given by the ratios of C to Si multiples lying between 6.8 and 16.1. This study shows significantly different multiple fractions for C and metal ions, respectively (see Table 1). This might be the reason for the worsening of the C composition compared to the LEAP 3000X HR instruments. In contrast to that, the GLE runs of both LEAP generations display similar C compositions of about 40 at%.

To get an indication for the underlying reason for the discrepancy in C composition between the generations of LEAP instruments, especially the role of laser wavelength, voltage runs on both instruments with steel samples including Cr-rich carbides were compared. The fraction of multiples in carbide subsets is presented in Table 3 and reconstructed volumes are presented in the Supplementary Material. One measurement was conducted with virtually the same parameters at 80 K test temperature. The fraction of ions in multi-hit events is consistently higher for the newer instrument. This was similarly reported by Martin et al. (2017) for a LEAP 5000 XR. Additional runs were performed at higher detection rates at 70 K. These runs show another increase in the fraction of

Table 3. Fraction of ions in multiple events for voltage NLE runs of steel samples within Cr-rich carbides.

Instrument	Parameters	C	V	Cr	Fe	Mo
LEAP 3000X HR	80 K, 0.2% DR	80.8	47.1	37.1	10.2	69.7
LEAP 6000 XR	80 K, 0.28% DR	85.0	51.9	42.4	12.7	74.6
LEAP 6000 XR	70 K, 0.5% DR	91.6	59.6	50.8	16.6	78.5
LEAP 6000 XR	70 K, 1% DR	91.4	61.0	49.8	16.9	81.0

ions in multi-hits. The influence of detection rate is however rather insignificant. The electrostatic field estimate is within 0.21 V/nm for the carbide regions of all voltage experiments. The fraction of ions in multi-hit events is similar between metal and C ions alike. This contrasts with the multiple fractions during laser runs as shown above and indicates that the different laser wavelengths have a significant impact on the evaporation mode of metal ions. This might in turn influence the resolution of the carbide/matrix interface as a higher field difference was documented for the LEAP 6000 XR than the LEAP 3000X HR measurements. An in-depth investigation into this phenomenon as well as the influence of possibly different heating of material constituents by the different wavelengths is desired but outside the scope of this work.

Conclusions

In this work, the newest generation of LEAP instrument, the LEAP 6000 XR, was employed with and without hardware filtering in the ion flight path to measure the accuracy of C composition measurements of Mo/V-containing MC carbides. The same steel sample material was used as in a previous study, allowing for a direct comparison between LEAP generations. A larger discrepancy to the expected C composition of 50 at% was found for the newer instrument. This could be explained by a lower fraction of metal ions in multi-hit events than before. The use of a hardware filter in the ion flight path significantly reduces multi-hit events and results in a more accurate C composition, as in previous studies. A higher laser pulse energy seems to increase the accuracy of C composition, which correlates with a decreasing number of multiples. The comparison of multiple ions in voltage runs indicates a difference in laser–matter interaction for the different laser wavelengths. The reduction of detection efficiency via a hardware filter is applicable to any element or compound with preferential loss due to multi-hit events.

Availability of Data and Materials

Datasets are available upon request.

Supplementary Material

To view supplementary material for this article, please visit https://doi.org/10.1093/mam/ozae069.

Acknowledgments

The experiments were performed at Chalmers Materials Analysis Laboratory (CMAL).

Financial Support

The authors gratefully acknowledge funding by the Swedish Research Council (2021-05072).

Conflict of Interest

The authors declare that they have no competing interest.

References

Andersson J (2011). *Secondary Hardening in Some Low-Chromium Hotwork Tool Steels*. Gothenburg: Chalmers University of Technology.

Baik SI, Isheim D & Seidman DN (2018). Systematic approaches for targeting an atom-probe tomography sample fabricated in a thin TEM specimen: Correlative structural, chemical and 3-D reconstruction analyses. *Ultramicroscopy* **184**, 284–292. https://doi.org/10.1016/j.ultramic.2017.10.007

Cuduvally R, Guergis B, Langelier B, Bassim ND, Andrei CM, Casagrande T, Arcuri GA & Russel S (2023). A correlative study of silicon carbide power devices using atom probe tomography and transmission electron microscopy. In: Conference Proceedings from the 49th International Symposium for Testing and Failure Analysis, November 12-16 2023, Phoenix Arizona USA, ASM International, p500–508. https://doi.org/1031339/asm.cp.istfa2023p0500

Da Costa G, Vurpillot F, Bostel A, Bouet M & Deconihout B (2005). Design of a delay-line position-sensitive detector with improved performance. *Rev Sci Instrum* **76**(1), 013304. https://doi.org/10.1063/1.1829975

Da Costa G, Wang H, Duguay S, Bostel A, Blavette D & Deconihout B (2012). Advance in multi-hit detection and quantization in atom probe tomography. *Rev Sci Instrum* **83**(12), 174504. https://doi.org/10.1063/1.4770120

De Geuser F, Gault B, Bostel A & Vurpillot F (2007). Correlated field evaporation as seen by atom probe tomography. *Surf Sci* **601**(2), 536–543. https://doi.org/10.1016/j.susc.2006.10.019

Gault B, Danoix F, Hoummada K, Mangelinck D & Leitner H (2012). Impact of directional walk on atom probe microanalysis. *Ultramicroscopy* **113**, 182–191. https://doi.org/10.1016/j.ultramic.2011.06.005

Gault B, Müller M, La Fontaine A, Moody MP, Shariq A, Cerezo A, Ringer SP & Smith GDW (2010). Influence of surface migration on the spatial resolution of pulsed laser atom probe tomography. *J Appl Phys* **108**(4), 044904. https://doi.org/10.1063/1.3462399

Hyde JM, Burke MG, Gault B, Saxey DW, Styman P, Wilford KB & Williams TJ (2011). Atom probe tomography of reactor pressure vessel steels: An analysis of data integrity. *Ultramicroscopy* **111**(6), 676–682. https://doi.org/10.1016/j.ultramic.2010.12.033

Ismail IM, Barat M, Brenot JC, Fayeton JA, Lepère V & Picard YJ (2005). A zero dead-time, multihit, time and position sensitive detector based on micro-channel plates. *Rev Sci Instrum* **76**(4), 043304. https://doi.org/10.1063/1.1889326

Jakob S, Hörnqvist Colliander M, Kawser J, Rashidi S, Ooi SW & Thuvander M (2024). Concomitant precipitation of intermetallic β-NiAl and carbides in a precipitation hardened steel. *Metall Mater Trans Phys Metall Mater Sci* **55**(3), 870–879. https://doi.org/10.1007/s11661-023-07291-7

Kingham DR (1982). The post-ionization of field evaporated ions: A theoretical explanation of multiple charge states. *Surf Sci* **116**(2), 273–301. https://doi.org/10.1016/0039-6028(82)90434-4

Kinno T, Akutsu H, Tomita M, Kawanaka S, Sonehara T, Hokazono A, Renaud L, Martin I, Benbalagh R, Sallé B & Takeno S (2012). Influence of multi-hit capability on quantitative measurement of NiPtSi thin film with laser-assisted atom probe tomography. *Appl*

Surf Sci **259**, 726–730. https://doi.org/10.1016/j.apsusc.2012.07.108

Kitaguchi HS, Lozano-Perez S & Moody MP (2014). Quantitative analysis of carbon in cementite using pulsed laser atom probe. *Ultramicroscopy* **147**, 51–60. https://doi.org/10.1016/j.ultramic.2014.06.004

Larson DJ, Prosa TJ, Ulfig RM, Geiser BP & Kelly TF (2013). *Local Electrode Atom Probe Tomography - A User's Guide*. New York, Heidelberg, Dordrecht, London: Springer. https://doi.org/10.1007/978-1-4614-8721-0

Lefebvre-Ulrikson W, Vurpillot F & Sauvage X (2016) *Atom Probe Tomography: Put Theory Into Practise*. London: Academic Press.

Leitner H, Stiller K, Andren HO & Danoix F (2004). Conventional and tomographic atom probe investigations of secondary-hardening carbides. *Surf Interface Anal* **36**(5–6 SPEC. ISS.), 540–545. https://doi.org/10.1002/sia.1695

Lewis JB, Isheim D, Floss C & Seidman DN (2015). $^{12}C/^{13}C$-ratio determination in nanodiamonds by atom-probe tomography. *Ultramicroscopy* **159**, 248–254. https://doi.org/10.1016/j.ultramic.2015.05.021

Mancini L, Amirifar N, Shinde D, Blum I, Gilbert M, Vella A, Vurpillot F, Lefebvre W, Lardé R, Talbot E, Pareige P, Portier X, Ziani A, Davesnne C, Durand C, Eymery J, Butté R, Carlin JF, Grandjean N & Rigutti L (2014). Composition of wide bandgap semiconductor materials and nanostructures measured by atom probe tomography and its dependence on the surface electric field. *J Phys Chem C* **118**(41), 24136–24151. https://doi.org/10.1021/jp5071264

Marceau RKW, Choi P & Raabe D (2013). Understanding the detection of carbon in austenitic high-Mn steel using atom probe tomography. *Ultramicroscopy* **132**, 239–247. https://doi.org/10.1016/j.ultramic.2013.01.010

Martin TL, London AJ, Jenkins B, Hopkin SE, Douglas JO, Styman PD, Bagot PAJ & Moody MP (2017). Comparing the consistency of atom probe tomography measurements of small-scale segregation and clustering between the LEAP 3000 and LEAP 5000 instruments. *Microsc Microanal* **23**(2), 227–237. https://doi.org/10.1017/S1431927617000356

Meisenkothen F, Steel EB, Prosa TJ, Henry KT & Prakash Kolli R (2015). Effects of detector dead-time on quantitative analyses involving boron and multi-hit detection events in atom probe tomography. *Ultramicroscopy* **159**(P1), 101–111. https://doi.org/10.1016/J.ULTRAMIC.2015.07.009

Miller MK & Forbes RG (2014). *Atom-Probe Tomography: The Local Electrode Atom Probe*. New York, Heidelberg, Dordrecht, London: Springer. https://doi.org/10.1007/978-1-4899-7430-3

Miller MK & Hetherington MG (1991). Local magnification effects in the atom probe. *Surf Sci* **246**(1–3), 442–449. https://doi.org/10.1016/0039-6028(91)90449-3

Morris RJH, Cuduvally R, Lin JR, Zhao M, Vandervorst W, Thuvander M & Fleischmann C (2022). Field dependent study on the impact of co-evaporated multihits and ion pile-up for the apparent stoichiometric quantification of GaN and AlN. *Ultramicroscopy* **241**, 113592. https://doi.org/10.1016/j.ultramic.2022.113592

Müller M, Gault B, Smith GDW & Grovenor CRM (2011). Accuracy of pulsed laser atom probe tomography for compound semiconductor analysis. *J Phys Conf Ser* **326**(1), 012031. https://doi.org/10.1088/1742-6596/326/1/012031

Peng Z, Choi PP, Gault B & Raabe D (2017). Evaluation of analysis conditions for laser-pulsed atom probe tomography: Example of cemented tungsten carbide. *Microsc Microanal* **23**(2), 431–442. https://doi.org/10.1017/S1431927616012654

Peng Z, Vurpillot F, Choi PP, Li Y, Raabe D & Gault B (2018). On the detection of multiple events in atom probe tomography. *Ultramicroscopy* **189**, 54–60. https://doi.org/10.1016/j.ultramic.2018.03.018

Prosa TJ & Oltman E (2022). Study of LEAP® 5000 deadtime and precision via silicon pre-sharpened-Microtip™ standard specimens. *Microsc Microanal* **28**(4), 1019–1037. https://doi.org/10.1017/S143192762101206X

Rolander U & Andrén H-O (1989). Statistical correction for pile-up in the atom-probe detector system. *Le J Phys Colloq* **50**(C8), C8-529–C8–534. https://doi.org/10.1051/jphyscol:1989891

Rolander U, & Andrén HO (1994). Study of proper conditions for quantitative atom-probe analysis. *Appl Surf Sci*, **76–77**(C), 392–402. https://doi.org/10.1016/0169-4332(94)90372-7

Schiester M, Waldl H, Hans M, Thuvander M, Primetzhofer D, Schalk N & Tkadletz M (2024). Influence of multiple detection events on compositional accuracy of TiN coatings in atom probe tomography. *Surf Coat Technol* **477**(September 2023), 130318. https://doi.org/10.1016/j.surfcoat.2023.130318

Stephan T, Heck PR, Isheim D & Lewis JB (2015). Correction of dead time effects in laser-induced desorption time-of-flight mass spectrometry: Applications in atom probe tomography. *Int J Mass Spectrom* **379**, 46–51. https://doi.org/10.1016/j.ijms.2014.12.006

Stephenson LT, Moody MP, Gault B & Ringer SP (2011). Estimating the physical cluster-size distribution within materials using atom-probe. *Microsc Res Tech* **74**(9), 799–803. https://doi.org/10.1002/jemt.20958

Takahashi J, Kawakami K & Kobayashi Y (2011). Quantitative analysis of carbon content in cementite in steel by atom probe tomography. *Ultramicroscopy* **111**(8), 1233–1238. https://doi.org/10.1016/j.ultramic.2011.03.024

Tang F, Gault B, Ringer SP & Cairney JM (2010). Optimization of pulsed laser atom probe (PLAP) for the analysis of nanocomposite Ti–Si–N films. *Ultramicroscopy* **110**(7), 836–843. https://doi.org/10.1016/j.ultramic.2010.03.003

Tegg L, Stephenson LT, & Cairney JM (2024). Estimation of the electric field in atom probe tomography experiments using charge state ratios. arXiv:2401.07989. http://arxiv.org/abs/2401.07989

Thuvander M, Kvist A, Johnson LJS, Weidow J & Andrén HO (2013). Reduction of multiple hits in atom probe tomography. *Ultramicroscopy* **132**, 81–85. https://doi.org/10.1016/j.ultramic.2012.12.005

Thuvander M, Shinde D, Rehan A, Ejnermark S & Stiller K (2019). Improving compositional accuracy in APT analysis of carbides using a decreased detection efficiency. *Microsc Microanal* **25**(2), 454–461. https://doi.org/10.1017/S1431927619000424

Thuvander M, Weidow J, Angseryd J, Falk J, Liu LKL, Sonestedt F, Stiller M, & Andrén K & O H (2011). Quantitative atom probe analysis of carbides. *Ultramicroscopy* **111**(6), 604–608. https://doi.org/10.1016/j.ultramic.2010.12.024

Vurpillot F, Bostel A & Blavette D (2000). Trajectory overlaps and local magnification in three-dimensional atom probe. *Appl Phys Lett* **76**(21), 3127–3129. https://doi.org/10.1063/1.126545

Yao L, Gault B, Cairney JM & Ringer SP (2010). On the multiplicity of field evaporation events in atom probe: A new dimension to the analysis of mass spectra. *Philos Mag Lett* **90**(2), 121–129. https://doi.org/10.1080/09500830903472997